

# Visualization of clustered protocadherin neuronal self-recognition complexes

Julia Brasch<sup>1,2,3,10</sup>, Kerry M. Goodman<sup>1,3,10</sup>, Alex J. Noble<sup>2</sup>, Micah Rapp<sup>1,2,3</sup>, Seetha Manneppalli<sup>1,3</sup>, Fabiana Bahna<sup>1,4,5</sup>, Venkata P. Dandey<sup>2</sup>, Tristan Bepler<sup>6,7</sup>, Bonnie Berger<sup>7,8</sup>, Tom Maniatis<sup>1,3</sup>, Clinton S. Potter<sup>2,3</sup>, Bridget Carragher<sup>2,3</sup>, Barry Honig<sup>1,3,4,5,9\*</sup> & Lawrence Shapiro<sup>1,3,5\*</sup>

**Neurite self-recognition and avoidance are fundamental properties of all nervous systems<sup>1</sup>.** These processes facilitate dendritic arborization<sup>2,3</sup>, prevent formation of autapses<sup>4</sup> and allow free interaction among non-self neurons<sup>1,2,4,5</sup>. Avoidance among self neurites is mediated by stochastic cell-surface expression of combinations of about 60 isoforms of  $\alpha$ -,  $\beta$ - and  $\gamma$ -clustered protocadherin that provide mammalian neurons with single-cell identities<sup>1,2,4–13</sup>. Avoidance is observed between neurons that express identical protocadherin repertoires<sup>2,5</sup>, and single-isoform differences are sufficient to prevent self-recognition<sup>10</sup>. Protocadherins form isoform-promiscuous *cis* dimers and isoform-specific homophilic *trans* dimers<sup>10,14–20</sup>. Although these interactions have previously been characterized in isolation<sup>15,17–20</sup>, structures of full-length protocadherin ectodomains have not been determined, and how these two interfaces engage in self-recognition between neuronal surfaces remains unknown. Here we determine the molecular arrangement of full-length clustered protocadherin ectodomains in single-isoform self-recognition complexes, using X-ray crystallography and cryo-electron tomography. We determine the crystal structure of the clustered protocadherin  $\gamma$ B4 ectodomain, which reveals a zipper-like lattice that is formed by alternating *cis* and *trans* interactions. Using cryo-electron tomography, we show that clustered protocadherin  $\gamma$ B6 ectodomains tethered to liposomes spontaneously assemble into linear arrays at membrane contact sites, in a configuration that is consistent with the assembly observed in the crystal structure. These linear assemblies pack against each other as parallel arrays to form larger two-dimensional structures between membranes. Our results suggest that the formation of ordered linear assemblies by clustered protocadherins represents the initial self-recognition step in neuronal avoidance, and thus provide support for the isoform-mismatch chain-termination model of protocadherin-mediated self-recognition, which depends on these linear chains<sup>11</sup>.

We determined a low-resolution crystal structure of a full-length clustered protocadherin (cPCDH)  $\gamma$ B4 ectodomain, which comprises six extracellular cadherin domains (EC1 to EC6); this revealed an extended zipper-like assembly (Fig. 1, Extended Data Fig. 1, Extended Data Table 1). The  $\gamma$ B4 molecules form *cis* dimers through an asymmetric interaction between the EC5 and EC6 of one protomer and the EC6 of the other (Fig. 1a); head-to-tail *trans* interactions—mediated by EC1 to EC4—between distinct *cis* dimers in the crystal generate a one-dimensional zipper-like array (Fig. 1b). The *cis* and *trans* interactions are similar to those that have previously been observed in the crystal structures of cPCDH  $\gamma$ B fragments<sup>15–20</sup>. Root mean square deviations between aligned C $\alpha$  atoms are between 2 and 3 Å (Extended Data Fig. 2), which suggests that little conformational change is required for zipper formation. The *cis* dimers in the zipper are arranged as if

they emanate from two apposed membrane surfaces, and the array is regular and could theoretically propagate indefinitely.

Whereas the crystal structure of the cPCDH  $\gamma$ B4 ectodomain reveals a polymeric structure assembled from *cis* and *trans* interactions, previous analytical ultracentrifugation experiments have shown that complete cPCDH  $\gamma$ B ectodomains form dimers-of-dimers in solution<sup>15,18</sup>. To understand this difference, we determined the overall architecture of these cPCDH  $\gamma$ B6<sub>EC1–6</sub> ectodomains complexes in solution using single-particle cryo-electron tomography (cryo-ET) on purified full-length cPCDH  $\gamma$ B6<sub>EC1–6</sub> ectodomains<sup>21</sup> preserved in vitreous ice (Fig. 2, Extended Data Fig. 3, Supplementary Video 1). Sub-tomogram averaging yielded a 3D map (with a resolution that was calculated to be about 35 Å by Fourier shell correlation = 0.143), which showed an asymmetrical elongated ellipsoidal shape with readily distinguishable characteristics that closely resemble individual observed particles. In this map, extended cPCDH ectodomains appear to wrap around each other in the central regions, and to cross at the top and bottom (Fig. 2a). Two-dimensional class averages obtained from individual images provide

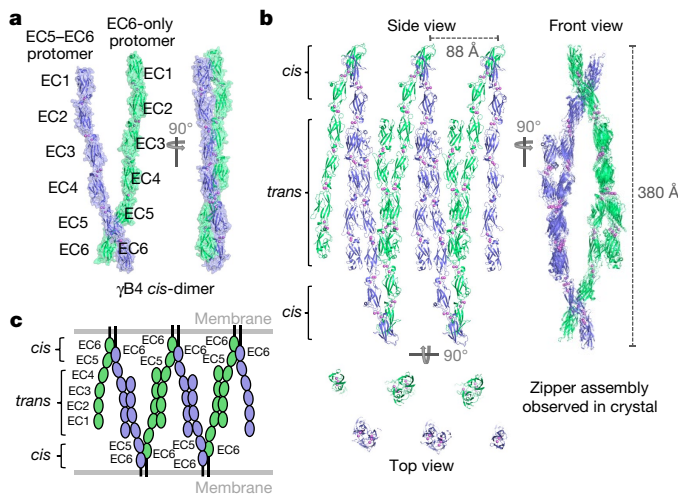


**Fig. 1 | Crystal structure of the cPCDH  $\gamma$ B4 ectodomain reveals a zipper-like assembly.** **a**, Asymmetric unit of the  $\gamma$ B4 crystal structure, which contains two  $\gamma$ B4<sub>EC1–6</sub> protomers (green and blue) engaged in the asymmetrical *cis*-dimer interaction. **b**, Zipper-like array of  $\gamma$ B4 through *trans* interactions mediated by EC1 to EC4, between *cis* dimers related by two-fold symmetry. Three orthogonal views are shown with bound calcium ions (violet spheres).  $\gamma$ B4 molecules that are interacting in *trans* are shown in identical colours. Top view shows a slice through the midsection. **c**, Schematic of the zipper-like assembly depicted in **b**, arranged as if between two membranes.

<sup>1</sup>Zuckerman Mind, Brain and Behavior Institute, Columbia University, New York, NY, USA. <sup>2</sup>Simons Electron Microscopy Center, New York Structural Biology Center, The National Resource for Automated Molecular Microscopy, New York, NY, USA. <sup>3</sup>Department of Biochemistry and Molecular Biophysics, Columbia University, New York, NY, USA. <sup>4</sup>Howard Hughes Medical Institute, Columbia University, New York, NY, USA. <sup>5</sup>Department of Systems Biology, Columbia University, New York, NY, USA. <sup>6</sup>Computational and Systems Biology, MIT, Cambridge, MA, USA. <sup>7</sup>Computer Science and Artificial Intelligence Laboratory, MIT, Cambridge, MA, USA. <sup>8</sup>Department of Mathematics, MIT, Cambridge, MA, USA. <sup>9</sup>Department of Medicine, Columbia University, New York, NY, USA. <sup>\*</sup>These authors contributed equally: Julia Brasch, Kerry M. Goodman. \*e-mail: bh6@cumc.columbia.edu; lss8@columbia.edu

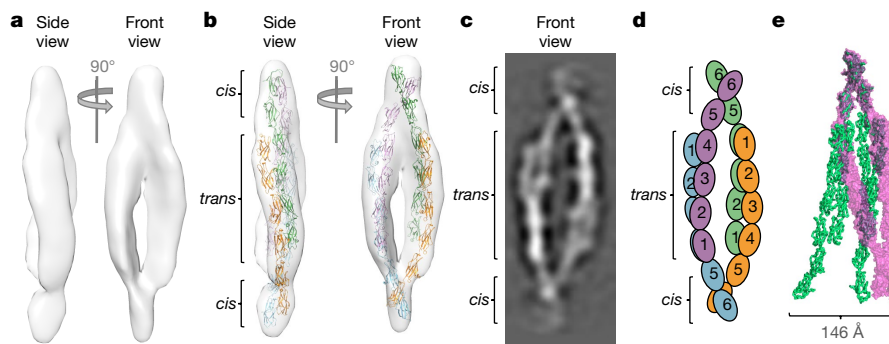


**Fig. 2 | cPCDH  $\gamma$ B6 ectodomains in solution assemble as a dimer-of-dimers through *cis* and *trans* interfaces.** **a**, Subtomogram-averaged density map of  $\gamma$ B6<sub>EC1-6</sub> particles from reconstructed tomograms reveals an asymmetric ellipsoidal complex. **b**, Fit of cPCDH  $\gamma$ B *trans*- and *cis*-dimer crystal structures into the cryo-ET map. **c**, Two-dimensional

class average of  $\gamma$ B6<sub>EC1-6</sub> particles in ice. Compare to **b**. **d**, Schematic of  $\gamma$ B6<sub>EC1-6</sub> ectodomains in the dimer-of-dimers. **e**, Overlay of  $\gamma$ B6<sub>EC1-6</sub> dimer-of-dimers (magenta volume) with  $\gamma$ B4<sub>EC1-6</sub> zipper from the crystal structure (green ribbon). Distance between the EC6 domains of equivalent protomers in each model indicated by a bracket.

domain-level resolution, and show the solution complex is a dimer of two bi-antennary *cis* dimers joined through *trans* binding interactions in each arm (Fig. 2c, Extended Data Fig. 4). Consistent with this configuration, the interacting EC5–6/EC6 regions of the  $\gamma$ B7<sub>EC3-6</sub> *cis*-dimer structure could readily be docked into the map (Fig. 2b). However, the EC3 and EC4 regions from the  $\gamma$ B7<sub>EC3-6</sub> structure did not fit within the map without allowing flexibility at the junction between EC4 and EC5, which suggests a conformational change relative to the fragment crystal structure (Extended Data Fig. 5, Extended Data Table 2). Similarly, fitting two copies of the *trans* dimer from the  $\gamma$ B2<sub>EC1-5</sub> crystal structure into the map necessitated bending and rotation of the *trans* dimers about the junction between EC2 and EC3; this was particularly pronounced in one of the two *trans*-dimer arms (Fig. 2b, Extended Data Fig. 5). These conformational differences with respect to the fragment crystal structures (Fig. 2e) facilitate the formation of a compact dimer-of-dimers in which all four protomers simultaneously engage in both *cis* and *trans* interactions<sup>20</sup> (Fig. 2b). The deformation of *cis*- and *trans*-dimer crystal structures required to form the dimer-of-dimers suggests that it may represent a high-energy conformation.

To determine whether dimer-of-dimers or zipper assemblies form between membranes, we tethered cPCDH  $\gamma$ B6 ectodomains to liposome surfaces<sup>22</sup> on which ectodomains could freely diffuse, mimicking a native membrane environment (Fig. 3a). Wild-type cPCDH  $\gamma$ B ectodomains mediated robust liposome aggregation, which was dependent on *trans* interactions (Fig. 3b), and mimicked cPCDH behaviour on cell surfaces<sup>10,14,15</sup> and in solution<sup>15</sup>. To visualize cPCDHs at membrane contact sites, we preserved wild-type  $\gamma$ B6<sub>EC1-6</sub> aggregates in vitreous ice and performed cryo-ET studies (Fig. 3c, Extended Data Fig. 6, Supplementary Videos 2, 3). Reconstructed tomograms revealed liposomes in contact with one another, and showed a constant intermembrane spacing of about 375 Å between parallel membranes as well as ordered protein density between adherent membranes. Different views of the cPCDH assembly were identifiable in the tomograms (Fig. 3c–e): an ellipsoid ‘front’ view that extended continuously through the volume of the tomogram (Extended Data Fig. 7, Supplementary Videos 2, 3); a striped, zipper-like ‘side’ view; and a dotted, regular, grid-like ‘top’ view that was evident in tomographic slices through cPCDH layers that connect vertically stacked liposomes. Visual comparison of  $\gamma$ B6<sub>EC1-6</sub> assemblies between membranes (Fig. 3c, e) with the cPCDH zipper observed in the crystal structure of  $\gamma$ B4<sub>EC1-6</sub> (Fig. 1) indicates a high level of correspondence; each of the major views that are evident in the tomogram are consistent with corresponding views of the zipper (Fig. 3c, e). cPCDHs thus form continuous ordered assemblies in a native-like membrane environment.

To determine the role of the *cis* interface we observed in our crystal structures, we repeated the cryo-ET experiments with the  $\gamma$ B6<sub>EC1-6</sub> *cis*-mutant V563D<sup>18</sup> on liposomes. As expected, because the *trans*

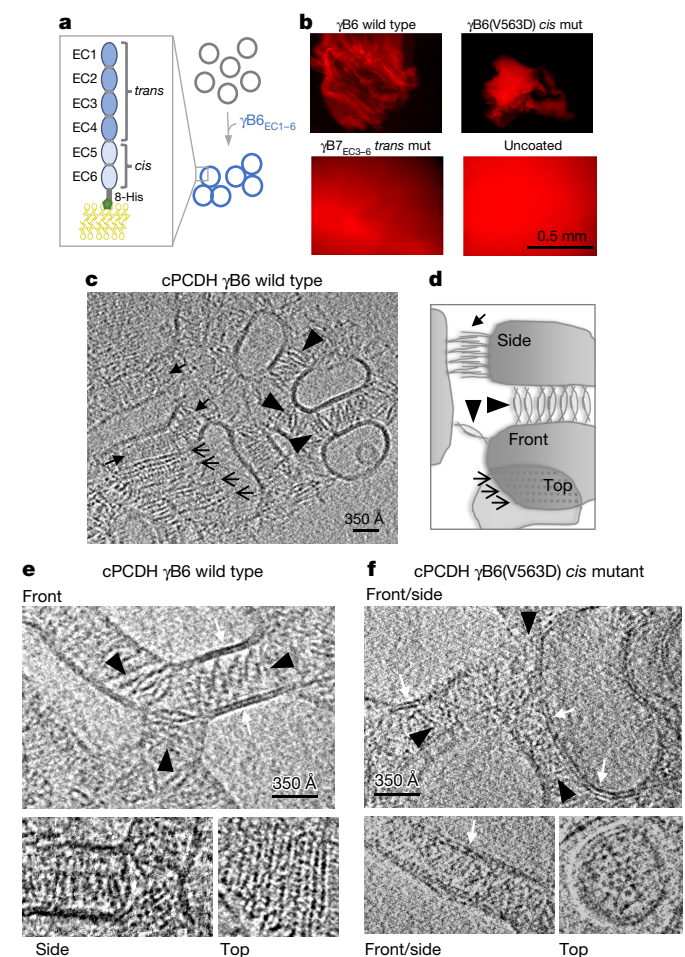


**Fig. 3 | cPCDH  $\gamma$ B6 forms continuous ordered assemblies between liposome membranes.** **a**,  $\gamma$ B6<sub>EC1-6</sub> ectodomains tethered to liposomes facilitate aggregation. **b**, Liposome aggregates visualized by fluorescence microscopy. Wild-type  $\gamma$ B6<sub>EC1-6</sub> and *cis*-mutant (mut) V563D both form single large aggregates, whereas the *trans*-mutant  $\gamma$ B7<sub>EC3-6</sub> does not aggregate liposomes. Negative control shows uncoated liposomes. **c**, Slice of a tomogram that shows aggregates of liposomes coated with wild-type  $\gamma$ B6<sub>EC1-6</sub> ectodomains. Different views of ordered assemblies indicated by arrows. **d**, Schematic of lattice orientations corresponding to views in **c**. **e**, **f**, Close-up views of individual slices of tomograms, showing front, side and top views of assemblies formed by ectodomains of wild-type  $\gamma$ B6<sub>EC1-6</sub> (**e**) and *cis*-mutant V563D (**f**). Note that ordered assemblies are absent in the mutant. White arrows indicate lipid bilayers.

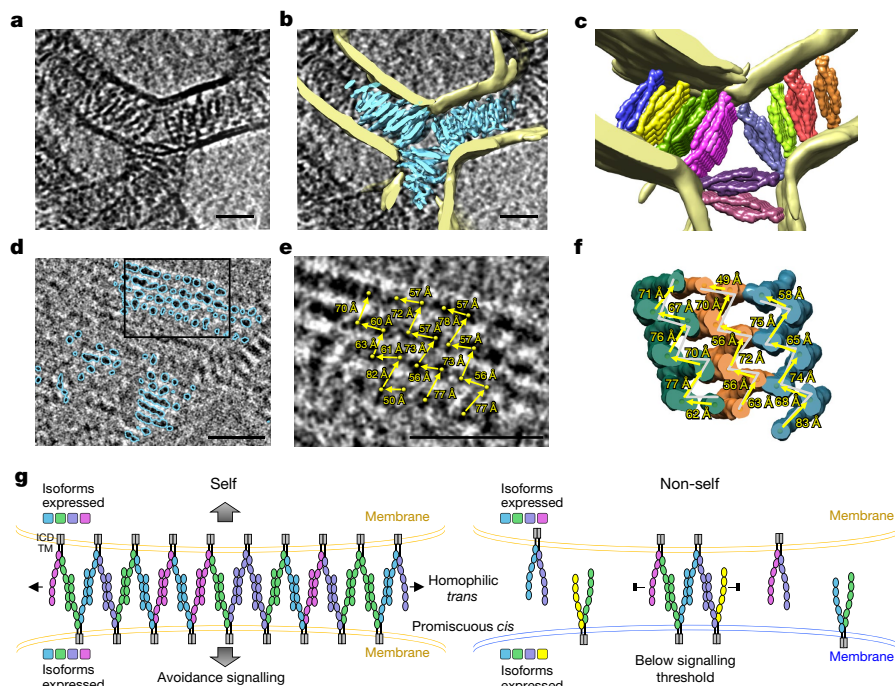


**Fig. 4 | cPCDH  $\gamma\text{B6}$  forms extended parallel zipper arrays on membranes, consistent with the chain-termination model.** **a**, Close-up view of a single tomographic slice that shows  $\gamma\text{B6}_{\text{EC1-6}}$  assemblies between liposome membranes. Parallel zipper arrays appear as front views extending into the plane (orthogonal to the zipper side view shown schematically in **g**). Scale bar, 350 Å. **b**, Annotated maps of lipid bilayers (yellow) and  $\gamma\text{B6}_{\text{EC1-6}}$  (cyan), overlaid on a slab on **a**. **c**, Ten linear arrays of *cis-trans* interactions from the  $\gamma\text{B4}_{\text{EC1-6}}$  crystal lattice (surfaces) fitted into the protein density. Lipid bilayers shown in yellow. See Supplementary

interface is intact, this mutant mediated liposome aggregation in a manner similar to wild-type  $\gamma\text{B6}_{\text{EC1-6}}$  (Fig. 3b). However, the characteristic ordered front, side and top views of the zipper-like arrays from wild-type experiments were absent (Fig. 3f, Supplementary Video 4), although ectodomains still accumulated at liposome contact sites in tomograms and single *trans* dimers could be observed. This demonstrates that ordered cPCDH assembly between membranes depends on the *cis* interactions we observed in crystal structures.

We next sought to characterize the correspondence between the crystallographic  $\gamma\text{B4}_{\text{EC1-6}}$  zipper and the intermembrane assembly we observed using cryo-ET. We fitted a portion of the  $\gamma\text{B4}_{\text{EC1-6}}$  zipper from the crystal structure into consecutive slices following a front-view array through the tomogram volume, which revealed a close correspondence between the crystal structure and the assembly from the tomogram (Extended Data Fig. 7).

To facilitate the docking of multiple crystallographic cPCDH  $\gamma\text{B4}_{\text{EC1-6}}$  zipper arrays into the density, we generated segmented maps for protein density and lipid bilayers using a convolutional neural network (Fig. 4a, b, d, Extended Data Fig. 8, Supplementary Video 5). Thirteen distinct zipper arrays—each comprising up to 14 *cis* dimers—were fitted into the protein density (Fig. 4c, f), with good correspondence to the segmented protein map (Supplementary Video 5). Top views of segmented maps that depict cPCDHs assembled between the apposed membranes of vertically stacked liposomes (Fig. 4d) revealed a repeating pattern in which distances measured between protomers mid-way through the zipper (Fig. 4e) alternated between short and long, with a notable correspondence to distances measured from the crystal structure (Fig. 4f). The average distance error between the lattices observed in the crystal structure and in the tomogram was  $< 3 \text{ \AA}$  ( $< 5\%$ ) for the three zippers we assessed. Neighbouring zipper assemblies are arranged such that they all propagate in parallel, which allows each to extend in an unimpeded manner (Fig. 4c, f). This parallel alignment could arise

Video 5. **d**, Tomogram slice showing annotated top views of parallel cPCDH zipper arrays (cyan) formed between membranes of vertically stacked liposomes. **e**, Magnification of the region boxed in **d**. Distances (arrows) between protomers (spheres) in three separate zipper arrays are given. **f**, Distances analogous to those in **e**, measured from zipper-array crystal structures fitted into the protein density. For comparison, distances from **e** are included as grey lines. **g**, Schematic of the chain-termination model of cPCDH function in neuronal self-avoidance. ICD, intracellular domain; TM, transmembrane domain.

owing to packing effects between the matching sawtooth structures of neighbouring zippers (Fig. 4e, f, Supplementary Video 5), but no consistent molecular interactions between the protomers of neighbouring zippers were observed.

The formation of zipper-like structures by cPCDHs between interacting membranes was previously hypothesized on the basis of *cis* and *trans* interactions revealed in biophysical studies<sup>15,17,18,20</sup>. Here we have shown that—despite the tendency of cPCDHs to form dimers-of-dimers in solution—a zipper-like lattice is the favoured assembly formed by cPCDH  $\gamma\text{B}$  ectodomains between interacting membrane surfaces. Because cPCDHs from all subfamilies have similar overall structures and use similar *cis* and *trans* interfaces<sup>15–20</sup>, all cPCDHs are likely to be able to incorporate into zipper-like arrays<sup>15,18</sup>. Although dimers-of-dimers were not observed in the tomographic volumes we analysed, we cannot rule out the possibility that this species could form between membranes when both arms of the interacting *cis* dimers are matched.

The assembly of cPCDHs into a zipper-like superstructure—in combination with the known homophilic specificity of *trans* interactions and promiscuity of *cis* interactions—underpins a chain-termination model for cPCDH-mediated discrimination between self and non-self<sup>11,15</sup>. In this model, large zipper assemblies can form between membrane surfaces that express identical subsets of cPCDH isoforms (for example, neurites from the same neuron), which triggers a signal that leads to avoidance (Fig. 4g). Our tomography results show that contiguous zippers extend the entire length of the contact region between membrane surfaces, and that neighbouring zippers can form in parallel to further increase the size of the assembly. By contrast, when isoform repertoires are not identical (for example, neurites from different neurons) mismatched isoforms are incorporated, which prevents the further growth of the zipper assemblies and limits their size below a presumed signalling threshold (Fig. 4g). Previous computational analyses have demonstrated that this mechanism can account for

discrimination between self and non-self among thousands of interacting neurons<sup>11,15,20</sup>.

Our results raise the question of whether the specific arrangement of cPCDH molecules in the zipper assembly is important for downstream signalling—for example, by coupling to structured elements in the cytoplasm—or, alternatively, whether the role of the zipper is simply to increase the concentration of cPCDHs at cell–cell contacts. Cell-based assays show that cPCDHs achieve high concentrations at contacts<sup>10</sup>, but it remains a critical question whether these concentrations are substantially lowered when mismatched isoforms are present and chains are terminated when they are short<sup>15</sup>. The details of the cPCDH-initiated signalling cascade that leads to neuronal avoidance<sup>5,23–27</sup> are not yet well-defined. Although cPCDH ectodomains are known to be cleaved by a metalloproteinase and  $\gamma$ -secretase<sup>28</sup>, it is unclear whether this function is involved in avoidance. Nevertheless, the structures of cPCDH recognition complexes reported here provide support for the chain-termination model for cPCDH-mediated self-recognition<sup>15</sup>, and a basis for future studies of the molecular mechanisms that underlie neuronal avoidance.

## Online content

Any methods, additional references, Nature Research reporting summaries, source data, statements of data availability and associated accession codes are available at <https://doi.org/10.1038/s41586-019-1089-3>.

Received: 3 July 2018; Accepted: 7 March 2019;

Published online 10 April 2019.

- Zipursky, S. L. & Grueber, W. B. The molecular basis of self-avoidance. *Annu. Rev. Neurosci.* **36**, 547–568 (2013).
- Lefebvre, J. L., Kostadinov, D., Chen, W. V., Maniatis, T. & Sanes, J. R. Protocadherins mediate dendritic self-avoidance in the mammalian nervous system. *Nature* **488**, 517–521 (2012).
- Molumby, M. J., Keeler, A. B. & Weiner, J. A. Homophilic protocadherin cell–cell interactions promote dendrite complexity. *Cell Reports* **15**, 1037–1050 (2016).
- Kostadinov, D. & Sanes, J. R. Protocadherin-dependent dendritic self-avoidance regulates neural connectivity and circuit function. *eLife* **4**, e08964 (2015).
- Mountoufaris, G. et al. Multicluster Pcdh diversity is required for mouse olfactory neural circuit assembly. *Science* **356**, 411–414 (2017).
- Wu, Q. & Maniatis, T. A striking organization of a large family of human neural cadherin-like cell adhesion genes. *Cell* **97**, 779–790 (1999).
- Wu, Q. et al. Comparative DNA sequence analysis of mouse and human protocadherin gene clusters. *Genome Res.* **11**, 389–404 (2001).
- Zipursky, S. L. & Sanes, J. R. Chemoaffinity revisited: dscams, protocadherins, and neural circuit assembly. *Cell* **143**, 343–353 (2010).
- Yagi, T. Molecular codes for neuronal individuality and cell assembly in the brain. *Front. Mol. Neurosci.* **5**, 45 (2012).
- Thu, C. A. et al. Single-cell identity generated by combinatorial homophilic interactions between  $\alpha$ ,  $\beta$ , and  $\gamma$  protocadherins. *Cell* **158**, 1045–1059 (2014).
- Rubinstein, R., Goodman, K. M., Maniatis, T., Shapiro, L. & Honig, B. Structural origins of clustered protocadherin-mediated neuronal barcoding. *Semin. Cell Dev. Biol.* **69**, 140–150 (2017).
- Toyoda, S. et al. Developmental epigenetic modification regulates stochastic expression of clustered protocadherin genes, generating single neuron diversity. *Neuron* **82**, 94–108 (2014).
- Ing-Esteves, S. et al. Combinatorial effects of alpha- and gamma-protocadherins on neuronal survival and dendritic self-avoidance. *J. Neurosci.* **38**, 2713–2729 (2018).
- Schreiner, D. & Weiner, J. A. Combinatorial homophilic interaction between  $\gamma$ -protocadherin multimers greatly expands the molecular diversity of cell adhesion. *Proc. Natl. Acad. Sci. USA* **107**, 14893–14898 (2010).
- Rubinstein, R. et al. Molecular logic of neuronal self-recognition through protocadherin domain interactions. *Cell* **163**, 629–642 (2015).
- Nicoludis, J. M. et al. Structure and sequence analyses of clustered protocadherins reveal antiparallel interactions that mediate homophilic specificity. *Structure* **23**, 2087–2098 (2015).
- Goodman, K. M. et al. Structural basis of diverse homophilic recognition by clustered  $\alpha$ - and  $\beta$ -protocadherins. *Neuron* **90**, 709–723 (2016).
- Goodman, K. M. et al.  $\gamma$ -Protocadherin structural diversity and functional implications. *eLife* **5**, e20930 (2016).
- Nicoludis, J. M. et al. Antiparallel protocadherin homodimers use distinct affinity- and specificity-mediating regions in cadherin repeats 1–4. *eLife* **5**, e18449 (2016).
- Goodman, K. M. et al. Protocadherin *cis*-dimer architecture and recognition unit diversity. *Proc. Natl. Acad. Sci. USA* **114**, E9829–E9837 (2017).
- Noble, A. J. et al. Routine single particle cryoEM sample and grid characterization by tomography. *eLife* **7**, e34257 (2018).
- Harrison, O. J. et al. The extracellular architecture of adherens junctions revealed by crystal structures of type I cadherins. *Structure* **19**, 244–256 (2011).
- Schalm, S. S., Ballif, B. A., Buchanan, S. M., Phillips, G. R. & Maniatis, T. Phosphorylation of protocadherin proteins by the receptor tyrosine kinase Ret. *Proc. Natl. Acad. Sci. USA* **107**, 13894–13899 (2010).
- Suo, L., Lu, H., Ying, G., Capecchi, M. R. & Wu, Q. Protocadherin clusters and cell adhesion kinase regulate dendrite complexity through Rho GTPase. *J. Mol. Cell Biol.* **4**, 362–376 (2012).
- Keeler, A. B., Schreiner, D. & Weiner, J. A. Protein kinase C phosphorylation of a  $\gamma$ -protocadherin c-terminal lipid binding domain regulates focal adhesion kinase inhibition and dendrite arborization. *J. Biol. Chem.* **290**, 20674–20686 (2015).
- Mah, K. M. & Weiner, J. A. Regulation of Wnt signalling by protocadherins. *Semin. Cell Dev. Biol.* **69**, 158–171 (2017).
- Fan, L. et al. Alpha protocadherins and Pyk2 kinase regulate cortical neuron migration and cytoskeletal dynamics via Rac1 GTPase and WAVE complex in mice. *eLife* **7**, e35242 (2018).
- Haas, I. G., Frank, M., Véron, N. & Kemler, R. Presenilin-dependent processing and nuclear function of  $\gamma$ -protocadherins. *J. Biol. Chem.* **280**, 9313–9319 (2005).

**Acknowledgements** We thank D. Neau, S. Banerjee and S. Narayanasami for help with synchrotron data collection, conducted at the APS NE-CAT 24-ID-C beamline (supported by National Institutes of Health (NIH) P41GM103403). We acknowledge support from a National Science Foundation grant (MCB-1412472) to B.H., NIH grants R01MH114817 to T.M. and L.S., F32GM128303 to A.J.N. and R01GM081871 to B.B. Electron microscopy was performed at the Simons Electron Microscopy Center (SEMC) and National Resource for Automated Molecular Microscopy located at the New York Structural Biology Center, which is supported by grants from the Simons Foundation (SF349247), NYSTAR and NIH (GM103310 and ODO19994) and from the Agouron Institute (F00316). We thank E. Eng and L.Y. Yen for technical support at SEMC.

**Reviewer information** *Nature* thanks Rob Meijers and the other anonymous reviewer(s) for their contribution to the peer review of this work.

**Author contributions** J.B., K.M.G., T.M., B.H. and L.S. designed experiments. J.B. performed liposome assays and all electron microscopy experiments. K.M.G. performed crystallography experiments. A.J.N. provided assistance with tomography imaging and with the reconstruction of the tomograms. S.M., F.B. and K.M.G. cloned, expressed and purified proteins. M.R. performed annotation of tomograms. V.P.D. prepared single-particle electron microscopy grids using Spotiton. T.B. and B.B. developed the neural-network particle picker. C.S.P. and B.C. oversaw the electron microscopy. B.H. and L.S. supervised the project. J.B. and K.M.G. prepared figures. J.B., K.M.G. and L.S. prepared the initial draft of the manuscript. J.B., K.M.G., A.J.N., T.M., C.S.P., B.C., B.H. and L.S. edited the manuscript.

**Competing interests** The authors declare no competing interests.

## Additional information

**Extended data** is available for this paper at <https://doi.org/10.1038/s41586-019-1089-3>.

**Supplementary information** is available for this paper at <https://doi.org/10.1038/s41586-019-1089-3>.

**Reprints and permissions information** is available at <http://www.nature.com/reprints>.

**Correspondence and requests for materials** should be addressed to B.H. or L.S. **Publisher's note:** Springer Nature remains neutral with regard to jurisdictional claims in published maps and institutional affiliations.

© The Author(s), under exclusive licence to Springer Nature Limited 2019

## METHODS

No statistical methods were used to predetermine sample size. The experiments were not randomized and investigators were not blinded to allocation during experiments and outcome assessment.

**Protein production.** cDNAs for mouse cPCDH ectodomain regions—excluding the predicted signal sequences—were cloned into a pLEXm mammalian expression vector (a kind gift from D. J. Leahy, John Hopkins University), modified with the BiP signal sequence and a C-terminal octahistidine tag<sup>16</sup>. The signal sequences were predicted using the SignalP 4.0 server<sup>29</sup>. cPCDH ectodomains consist of six extracellular cadherin domains, followed by an unstructured linker of 23–25 amino acids before the transmembrane helix<sup>21</sup>. The  $\gamma$ B4<sub>EC1–6</sub> and  $\gamma$ B6<sub>EC1–6</sub> constructs used in this study contain coding sequences for the six extracellular cadherin domains and five residues from the unstructured linker, followed by the octahistidine tag (residues 1–638 for  $\gamma$ B4<sub>EC1–6</sub>, following signal peptide cleavage, and residues 1–641 for  $\gamma$ B6<sub>EC1–6</sub>). cPCDH  $\gamma$ B4 and  $\gamma$ B6 share 67.1% sequence identity, and display similar *cis* and *trans* dimerization behaviour<sup>18</sup>. The  $\gamma$ B6<sub>EC1–6</sub> *cis*-mutant construct V563D was generated using the standard Quikchange mutagenesis protocol (Stratagene).

Suspension-adapted HEK293 Freestyle cells (Invitrogen) in serum-free medium (Invitrogen) were used for protein expression. The cell line was not tested for mycoplasma contamination and has not been authenticated. The plasmid constructs were transfected into cells using polyethyleneimine (Polysciences). Medium was collected ~6 days after transfection and the secreted proteins were purified by nickel-affinity chromatography followed by size-exclusion chromatography in 10 mM Tris pH 8.0, 150 mM sodium chloride, 3 mM calcium chloride, and 200–250 mM imidazole pH 8.0. Purified proteins were concentrated to >2 mg/ml and used for crystallization and/or electron microscopy experiments. Molecular masses determined by mass spectrometry (Iowa State University Mass Spectrometry Facility) for the purified wild-type proteins were 76.6 kDa for  $\gamma$ B4<sub>EC1–6</sub> and 77.7 kDa for  $\gamma$ B6<sub>EC1–6</sub>.

**X-ray crystallography.**  $\gamma$ B4<sub>EC1–6</sub> protein crystals were grown using protein in size-exclusion buffer (10 mM Tris pH 8.0, 150 mM sodium chloride, 3 mM calcium chloride and 200 mM imidazole), at a concentration of 3 mg/ml and using the vapour diffusion method. The crystallization condition was 10% (w/v) PEG8000, 20% ethylene glycol, 10% Morpheus Amino Acids (Molecular Dimensions) and 0.1 M Morpheus Buffer System 2 (Hepes/MOPS buffer; Molecular Dimensions), pH 7.5. X-ray diffraction data were collected at 100 K from a single crystal at Northeastern Collaborative Access Team (NE-CAT) beamline 24ID-C at the Advanced Photon Source, Argonne National Laboratory. The dataset was indexed using XDS<sup>30</sup> and scaled using XSSCALE<sup>30</sup>.

**Diffraction anisotropy.** The X-ray diffraction data showed strong diffraction anisotropy, with relatively strong diffraction along  $c^*$  and much weaker diffraction along  $a^*$  and  $b^*$  (Extended Data Fig. 1, Extended Data Table 1). These data were therefore truncated using ellipsoidal limits of 6.0, 6.8 and 4.5 Å along each of the three principal crystal axes, as implemented in the UCLA Diffraction Anisotropy Server<sup>31</sup>. The completeness within the applied ellipsoidal resolution limits was 93.6%.

**Crystal-structure phasing and refinement.** The  $\gamma$ B4<sub>EC1–6</sub> crystal structure was solved by molecular replacement using Phaser<sup>32</sup>, implemented in Phenix<sup>33</sup>, using the  $\gamma$ B7<sub>EC3–6</sub> *cis*-dimer structure (RCSB Protein Data Bank code (PDB) 5V5X)<sup>21</sup> as a search model. Following an initial round of rigid-body refinement using Phenix<sup>33</sup>, EC1 to EC2 from the  $\gamma$ B2<sub>EC1–5</sub> crystal structure (PDB 5T9T)<sup>19</sup> were manually placed using structural alignment of the EC3 to EC4 regions of the  $\gamma$ B2<sub>EC1–5</sub> crystal structure as a guide to the molecular replacement solution. The resulting model was subjected to a further round of rigid-body refinement. At this stage, there was clear difference density for the interdomain calcium ions and covalently linked glycans that were not present in the models (Extended Data Fig. 1). Iterative model building using Coot<sup>34</sup> and maximum-likelihood refinement using Phenix<sup>33</sup> was subsequently conducted, with care taken to maintain the geometry given the low resolution of the data; this yielded the final refined structure, the statistics of which are reported in Extended Data Table 1.

The electron density maps obtained were of reasonably good quality, given the low resolution (Extended Data Fig. 1). However, owing to this low resolution, atomic details were not well-defined and side chains were often not resolved. The local geometry of the starting models taken from higher-resolution published crystal structures of cPCDH  $\gamma$ B fragments was therefore maintained as much as possible. Given these resolution constraints, we have limited our discussion of the crystal structure to the overall architecture and arrangement of the molecules in the crystal.

**Structure analysis.** Interdomain angles were calculated using UCSF Chimera<sup>35</sup>. Root mean square deviations between aligned C $\alpha$  atoms between structures were calculated using PyMol (Schrödinger). Protein structure figures were made using PyMol or UCSF Chimera<sup>35</sup>.

**Sample preparation for single-particle cryo-electron microscopy.** Single-particle grids were prepared using Spotiton v.1.0 robot<sup>36–38</sup> to obtain thin vitreous ice, aiding contrast during data collection. Lacey carbon or gold nanowire grids were prepared in-house as previously described<sup>39</sup>. Grids were glow-discharged for 10 s with O<sub>2</sub> and H<sub>2</sub>, the sample was dispensed onto the grid in 50- $\mu$ l drops as one single stripe and incubated for ~500 ms as determined by the calibrated self-wicking time per grid, followed by plunging into liquid ethane.

**Liposome aggregation assay and sample preparation for cryo-ET experiments.** Liposomes were prepared by a hydration and extrusion method from an 8:2 molar ratio of 1,2-dioleoyl-sn-glycero-3-phosphocholine (DOPC) and the nickel salt of 1,2-dioleoyl-sn-glycero-3-[(N(5-amino-1-carboxypentyl)iminodiacetic acid)-succinyl] (DOGS-NTA) according to the manufacturer's protocol (Avanti Lipids). Lipids were hydrated with assay buffer (25 mM HEPES pH 7.4, 0.1 M KCl, 10% (v/v) glycerol and 3 mM CaCl<sub>2</sub>) and resuspended liposomes were extruded using membranes with a pore size of 100 nm. Liposome aggregation assays were adapted from previously described experiments<sup>22</sup>: liposomes and purified octahistidine-tagged cPCDH ectodomains were mixed at final concentrations of 10 mM liposomes and 7  $\mu$ M protein, in assay buffer, to a total volume of 20  $\mu$ l, and incubated at 37 °C for eight hours. When cells that express cPCDHs come into contact with one another, all detectable cPCDH from the cell surface localizes to the site of cell-cell contact<sup>10</sup>; we see a similar effect with liposomes, and cPCDH zippers are observed even for low protein-coating densities (for example, Fig. 3c).

For electron microscopy experiments, large aggregates were gently resuspended by trituration with a 10- $\mu$ l pipette tip, and 3  $\mu$ l of each suspension were incubated on home-made, glow-discharged lacey carbon grids for 10 s at 85% relative humidity, blotted for 2.5 s and flash-frozen in liquid ethane using a semi-automated approach by using either a Gatan CP3 or FEI Vitrobot.

For fluorescence microscopy, liposomes were prepared with rhodamine lipids (Sigma) in addition to the standard composition of DOPC and DOGS-NTA. Assays were performed as described for electron microscopy, and 5  $\mu$ l of each experiment was imaged with a Nikon eclipse E800 microscope using QCapture.

**Tilt-series data collection.** Tilt-series were collected using a Titan Krios (FEI/Thermo Fisher) outfitted with a direct detector Gatan K2 (Gatan) at 300 keV. Some wild-type (Supplementary Video 3), and all *cis*-mutant,  $\gamma$ B6<sub>EC1–6</sub> tilt-series were collected using a Gatan Bioquantum energy filter (Gatan). In addition, two of nine single-particle tilt-series were collected using a Volta phase plate (FEI/Thermo Fisher). Data were collected bi-directionally with a tilt-range of −54° to 54° in 2° increments using Leginon<sup>40,41</sup> with 100-ms frames for each tilt image at a nominal defocus range of 0 and 2 (phase plate collections) or 6 micrometres. Total dose per tilt-series collected was between 50 and 150 e<sup>−</sup> per Å<sup>2</sup> with dose rates of approximately 8 e<sup>−</sup> per pixel per s. Incident dose for the 0° tilt image was between 1.5 and 3.0 e<sup>−</sup> per Å<sup>2</sup>, and increased for higher tilt angles according to the cosine of the tilt angle. Single-particle tilt-series were collected at a pixel size of 1.76 Å and tilt-series of cPCDH-coated liposomes at 1.84 Å. Full-frame alignment was performed using MotionCor<sup>42</sup>.

**Tilt-series alignment.** Tilt-series were aligned using Appion-Protomo<sup>43–45</sup>. Tilt-series were coarsely aligned, manually aligned and then refined using a set of alignment thicknesses. The best-aligned iteration was reconstructed for visual analysis using Tomo3D SIRT<sup>46,47</sup> after dose compensation using a previously described relation<sup>48</sup>. CTF correction was not performed.

**Sub-tomogram averaging of the dimers-of-dimers.** Particle picking was performed using the dipole set model in Dynamo<sup>49,50</sup>. Each particle of a dimer-of-dimers was annotated at the termini with ‘north’ and ‘south’ to pre-define the long axis and aid sub-tomogram alignment (Extended Data Fig. 3). In 7 tomograms, 506 particles were annotated, sub-volumes extracted and processed through sub-tomogram alignment and refinement using Dynamo<sup>49,50</sup>. An initial model was created from 86 randomly chosen particles and an ellipsoid mask was applied during refinement. Azimuth and cone flip were both enabled to allow particles to flip 180° during refinement to permit correction of inverted dipole annotation. No symmetry was applied because tests using two-fold symmetry resulted in featureless maps, which is consistent with the non-identical bend and rotation apparent in the two *trans*-dimer regions of the final map (Fig. 1).

**Single-particle 2D data collection and processing.** Data were collected at 300 kV on a Titan Krios (FEI/Thermo Fisher) equipped with a Gatan K2 Counting camera. The pixel size was 1.1 Å and defocus ranged from 1–4 micrometres. Exposures were set to 10 s (40 frames per image) for a total dose of ~68 e<sup>−</sup> per Å<sup>2</sup>. Frames were aligned using MotionCor<sup>42</sup>. One thousand, five hundred and forty particles were picked manually from 87 micrographs using Appion Manual Picker<sup>44</sup> to serve as a training set for a positive-unlabelled convoluted neural-network particle picker, Topaz<sup>51</sup>. Fourteen thousand, five hundred and sixty-nine particles were selected and 2D classification was performed in Relion2<sup>52</sup>, which provided domain-level resolution. Strong preferred orientation was shown in the 2D-class averages, and single-particle tomograms revealed that cPCDH  $\gamma$ B6<sub>EC1–6</sub> was predominantly

localized to the air–water interface<sup>23</sup>. As a result, we pursued further 3D reconstruction using cryo-ET.

**Neural-network tomogram annotation.** Semi-automated segmentation of the tomograms was performed using the TomoSeg protocol in EMAN2.2<sup>53</sup>. Tomograms were imported into the EMAN2.2 workflow, and binned for a final pixel size of 7.36 Å. For annotation of cPCDH density, thirteen 64 × 64 pixel regions of interest were selected from the reconstructed tomogram and manually annotated as positive training references, and 123 regions of interest were selected as negative training references. For annotation of liposome membrane density, 10 regions of interest were selected and manually annotated as positive training references, and 100 regions of interest were selected as negative training references. Convolutional neural-network training was performed with the default parameters of EMAN2.2 for lipid bilayers, and the cPCDH convolutional neural network was trained over 40 iterations.

**Fitting of continuous  $\gamma$ B4<sub>EC1–6</sub> arrays into annotated tomogram maps.** Atomic models were fit into the annotated tomogram using the FitMap command in UCSF Chimera<sup>35</sup>. The tomogram was examined by eye to determine the length of the lattices that formed between liposome membranes and the lattice assembly of the crystal structure of  $\gamma$ B4<sub>EC1–6</sub> was extended to match the continuous density. The structural assembly was placed in the intermembrane space, and fit globally within a 50-nm radius of the initial placement. The average correlation coefficient at 20 Å was 0.735 ± 0.0305.

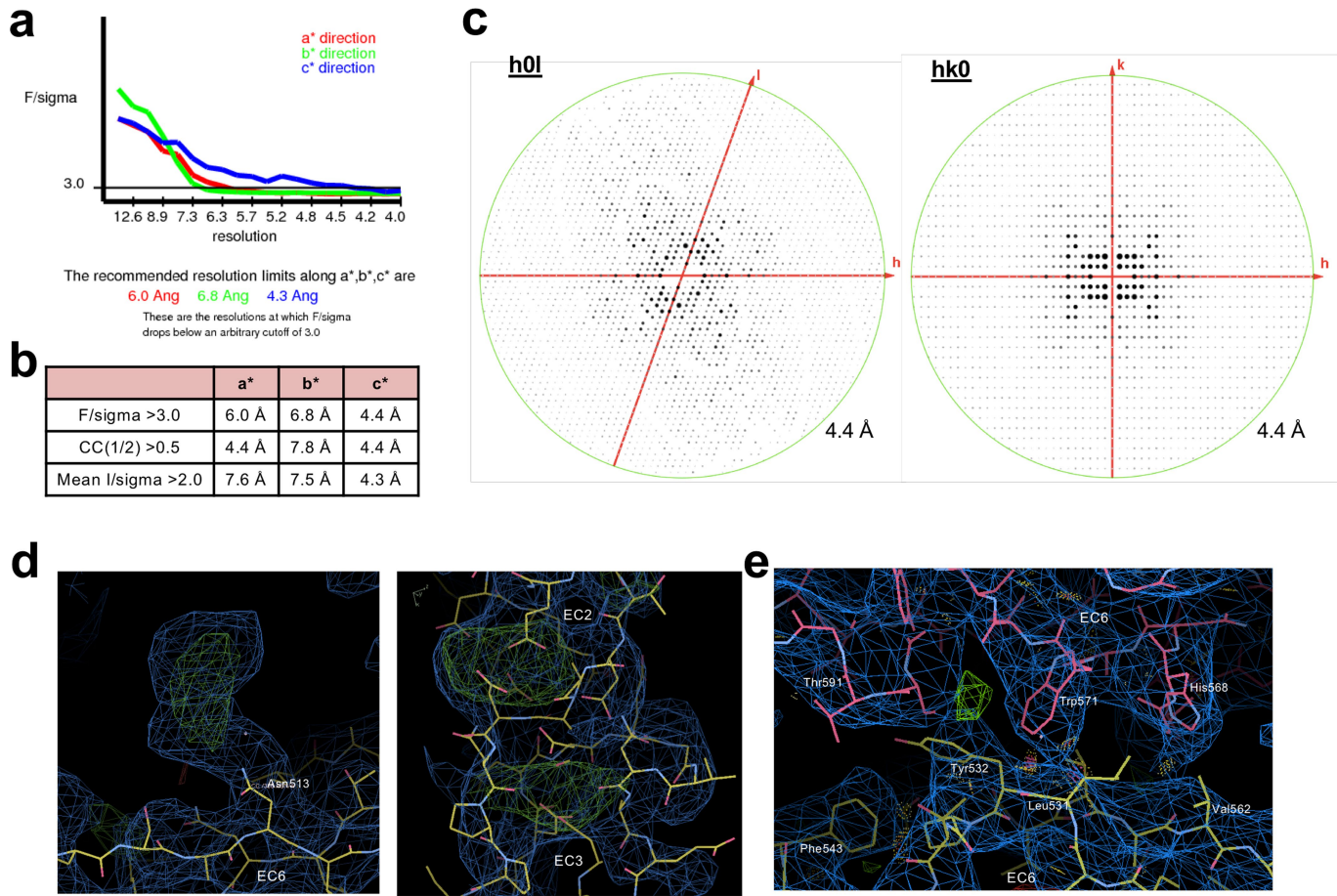
**Statistics and reproducibility.** The crystal structure was determined from diffraction data obtained from one crystal ( $n = 1$ ; Extended Data Fig. 1a, c). Multiplicity and final refinement statistics are reported in Extended Data Table 1. The single-particle cryo-EM map of the dimer-of-dimers was determined using sub-tomogram averaging of volumes extracted from  $n = 7$  independent experiments (Fig. 2c, Extended Data Fig. 3). The single-particle averages shown in Fig. 2c and Extended Data Fig. 4 were highly reproducible from three independent experiments ( $n = 3$ ). Liposome aggregation assays for wild-type and mutant cPCDH were replicated in  $n = 3$  independent experiments, with highly consistent results (Figs. 3, 4, Extended Data Figs. 6–8). Reconstructed tomograms of wild-type and mutant proteins coated onto liposomes—of which representative images and regions of interest are shown in Figs. 2, 4, Extended Data Figs. 6–8—are derived from  $n > 4$  independent experiments. Ordered assemblies (Fig. 3c, e, 4a, d, Extended Data Figs. 6–8) were consistently observed in all wild-type cPCDH experiments ( $n > 11$ ), whereas the ordered assemblies were consistently absent in all *cis*-mutant cPCDH tilt series ( $n > 4$ , Fig. 3f). The neural-network segmentation of protein density and lipid bilayers was trained on the full tomogram shown (Extended Data Fig. 8a), and could reliably be applied to other tomograms ( $n = 2$ , Fig. 4a, b, d, e, Extended Data Fig. 8b).

**Reporting summary.** Further information on research design is available in the Nature Research Reporting Summary linked to this paper.

## Data availability



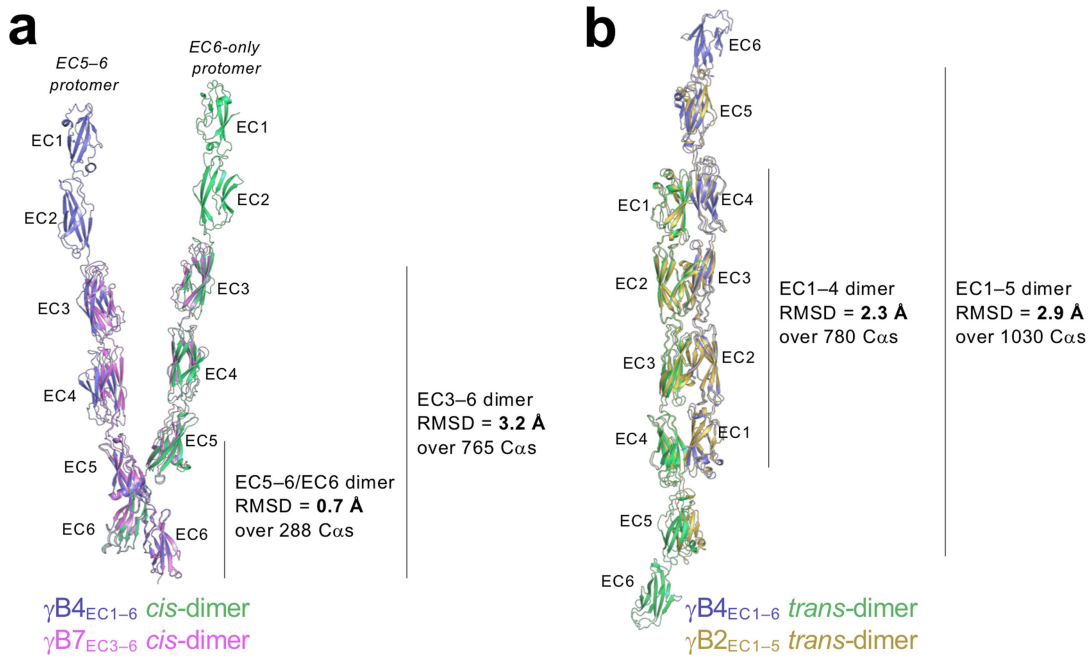
29. Petersen, T. N., Brunak, S., von Heijne, G. & Nielsen, H. SignalP 4.0: discriminating signal peptides from transmembrane regions. *Nat. Methods* **8**, 785–786 (2011).
30. Kabach, W. XDS. *Acta Crystallogr. D* **66**, 125–132 (2010).
31. Strong, M. et al. Toward the structural genomics of complexes: crystal structure of a PEP/PPE protein complex from *Mycobacterium tuberculosis*. *Proc. Natl. Acad. Sci. USA* **103**, 8060–8065 (2006).
32. McCoy, A. J. et al. Phaser crystallographic software. *J. Appl. Crystallogr.* **40**, 658–674 (2007).
33. Adams, P. D. et al. PHENIX: a comprehensive Python-based system for macromolecular structure solution. *Acta Crystallogr. D* **66**, 213–221 (2010).
34. Emsley, P., Lohkamp, B., Scott, W. G. & Cowtan, K. Features and development of Coot. *Acta Crystallogr. D* **66**, 486–501 (2010).
35. Pettersen, E. F. et al. UCSF Chimera—a visualization system for exploratory research and analysis. *J. Comput. Chem.* **25**, 1605–1612 (2004).
36. Jain, T., Sheehan, P., Crum, J., Carragher, B. & Potter, C. S. Spoton: a prototype for an integrated inkjet dispense and vitrification system for cryo-TEM. *J. Struct. Biol.* **179**, 68–75 (2012).
37. Dandey, V. P. et al. Spoton: New features and applications. *J. Struct. Biol.* **202**, 161–169 (2018).
38. Wei, H. et al. Optimizing “self-wicking” nanowire grids. *J. Struct. Biol.* **202**, 170–174 (2018).
39. Razinkov, I. et al. A new method for vitrifying samples for cryoEM. *J. Struct. Biol.* **195**, 190–198 (2016).
40. Suloway, C. et al. Automated molecular microscopy: the new Leginon system. *J. Struct. Biol.* **151**, 41–60 (2005).
41. Suloway, C. et al. Fully automated, sequential tilt-series acquisition with Leginon. *J. Struct. Biol.* **167**, 11–18 (2009).
42. Zheng, S. Q. et al. MotionCor2: anisotropic correction of beam-induced motion for improved cryo-electron microscopy. *Nat. Methods* **14**, 331–332 (2017).
43. Noble, A. J. & Stagg, S. M. Automated batch fiducial-less tilt-series alignment in Appion using Protomo. *J. Struct. Biol.* **192**, 270–278 (2015).
44. Lander, G. C. et al. Appion: an integrated, database-driven pipeline to facilitate EM image processing. *J. Struct. Biol.* **166**, 95–102 (2009).
45. Winkler, H. & Taylor, K. A. Accurate marker-free alignment with simultaneous geometry determination and reconstruction of tilt series in electron tomography. *Ultramicroscopy* **106**, 240–254 (2006).
46. Aguirreiro, J. I. & Fernandez, J. J. Fast tomographic reconstruction on multicore computers. *Bioinformatics* **27**, 582–583 (2011).
47. Aguirreiro, J.-I. & Fernandez, J.-J. Tomo3D 2.0—exploitation of advanced vector extensions (AVX) for 3D reconstruction. *J. Struct. Biol.* **189**, 147–152 (2015).
48. Grant, T. & Grigorieff, N. Measuring the optimal exposure for single particle cryo-EM using a 2.6 Å reconstruction of rotavirus VP6. *eLife* **4**, e06980 (2015).
49. Castaño-Díez, D., Kudryashev, M., Arheit, M. & Stahlberg, H. Dynamo: a flexible, user-friendly development tool for subtomogram averaging of cryo-EM data in high-performance computing environments. *J. Struct. Biol.* **178**, 139–151 (2012).
50. Castaño-Díez, D., Kudryashev, M. & Stahlberg, H. Dynamo Catalogue: geometrical tools and data management for particle picking in subtomogram averaging of cryo-electron tomograms. *J. Struct. Biol.* **197**, 135–144 (2017).
51. Bepler, T. et al. Positive-unlabeled convolutional neural networks for particle picking in cryo-electron micrographs. Preprint at <https://arxiv.org/abs/1803.08207> (2018).
52. Kiranius, D., Forsberg, B. O., Scheres, S. H. W. & Lindahl, E. Accelerated cryo-EM structure determination with parallelisation using GPUs in RELION-2. *eLife* **5**, e18722 (2016).
53. Chen, M. et al. Convolutional neural networks for automated annotation of cellular cryo-electron tomograms. *Nat. Methods* **14**, 983–985 (2017).
54. Evans, P. R. & Murshidov, G. N. How good are my data and what is the resolution? *Acta Crystallogr. D* **69**, 1204–1214 (2013).
55. Evans, P. Scaling and assessment of data quality. *Acta Crystallogr. D* **62**, 72–82 (2006).



**Extended Data Fig. 1 | X-ray diffraction anisotropy and electron density map quality for the low-resolution  $\gamma$ B4<sub>EC1-6</sub> crystal structure.**

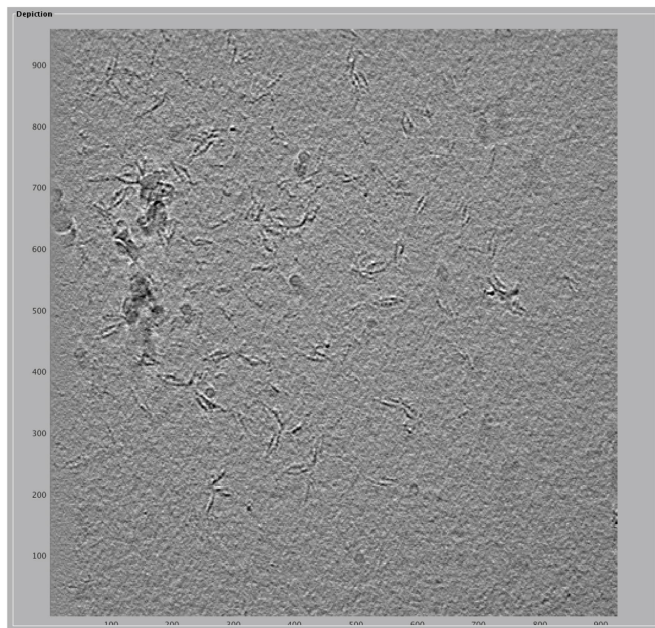
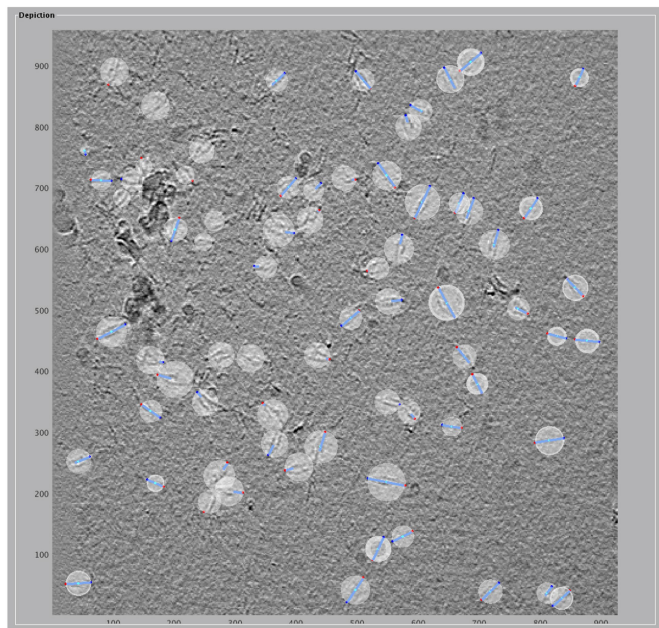
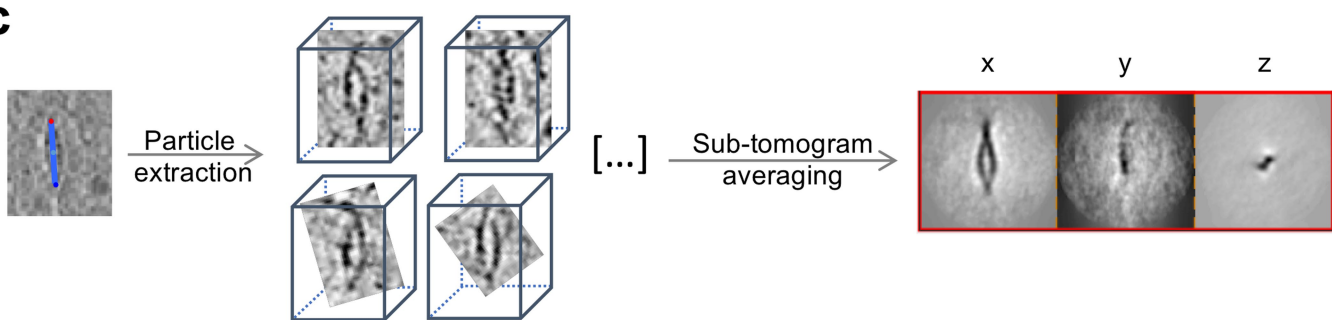
**a**, UCLA Diffraction Anisotropy Server<sup>31</sup> output showing the data strength as measured by  $F/\sigma$  along the  $a^*$ ,  $b^*$  and  $c^*$  axes. **b**, The diffraction limits along the  $a^*$ ,  $b^*$  and  $c^*$  axes determined by three different methods:  $F/\sigma$  from (a), and the correlation coefficient (CC) and  $I/\sigma$  limits calculated by Aimless<sup>54,55</sup>. **c**, Synthetic precession photographs of the X-ray diffraction in the  $k = 0$  plane (left) and the  $l = 0$  plane (right), showing the comparatively stronger or weaker diffraction. **d**, Examples of electron density images of the  $\gamma$ B4<sub>EC1-6</sub> crystal structure, highlighting the difference density observed for ligand molecules after placement

of all protein domains and one round of rigid-body refinement. Left, difference density for a glycosylated asparagine residue (Asn513, chain B). Right, difference density for the three calcium ions coordinated between extracellular cadherin domains (EC2-EC3 chain B).  $2F_o - F_c$  (blue) and  $F_o - F_c$  maps (green and red) are shown contoured at 1.0 and  $\pm 3.0\sigma$ , respectively. **e**, Example of electron density image of the  $\gamma$ B4<sub>EC1-6</sub> crystal structure after refinement, showing the *cis* interface. The EC5-EC6 protomer is coloured pink, and the EC6-only protomer is coloured yellow.  $2F_o - F_c$  (blue) and  $F_o - F_c$  maps (green and red) are shown contoured at 1.0 and  $\pm 3.0\sigma$ , respectively.



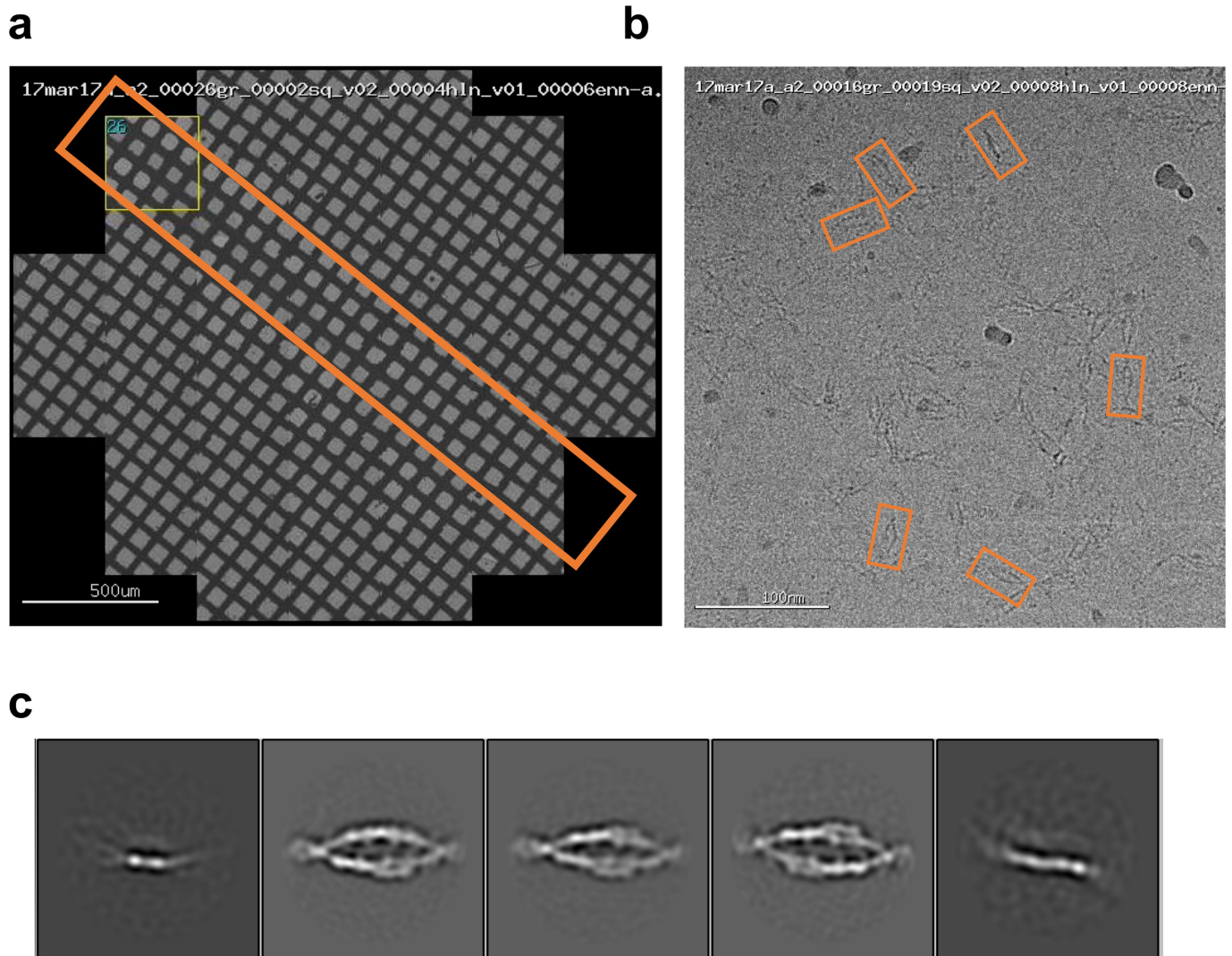
**Extended Data Fig. 2 | Comparison between the  $\gamma\text{B4}_{\text{EC1-6}}$  crystal structure and cPCDH  $\gamma\text{B}$  fragment structures reveals that the formation of the zipper assembly does not require large conformational changes.** **a**, Structural superposition of the  $\gamma\text{B4}_{\text{EC1-6}}$  *cis* dimer from the crystal structure (one protomer in slate ribbon, the other in green) with the  $\gamma\text{B7}_{\text{EC3-6}}$  fragment *cis*-dimer structure (PDB 5V5X; pink ribbon),

showing the overall similarity between the two structures (particularly in the EC5–6/EC6 *cis*-interacting regions). **b**, Structural superposition of the  $\gamma\text{B4}_{\text{EC1-6}}$  *trans* dimer from the crystal structure (slate and green ribbon) with the  $\gamma\text{B2}_{\text{EC1-5}}$  fragment *trans*-dimer structure (PDB 5T9T; gold ribbon), showing the overall similarity between the *trans* dimers.

**a****b****c**

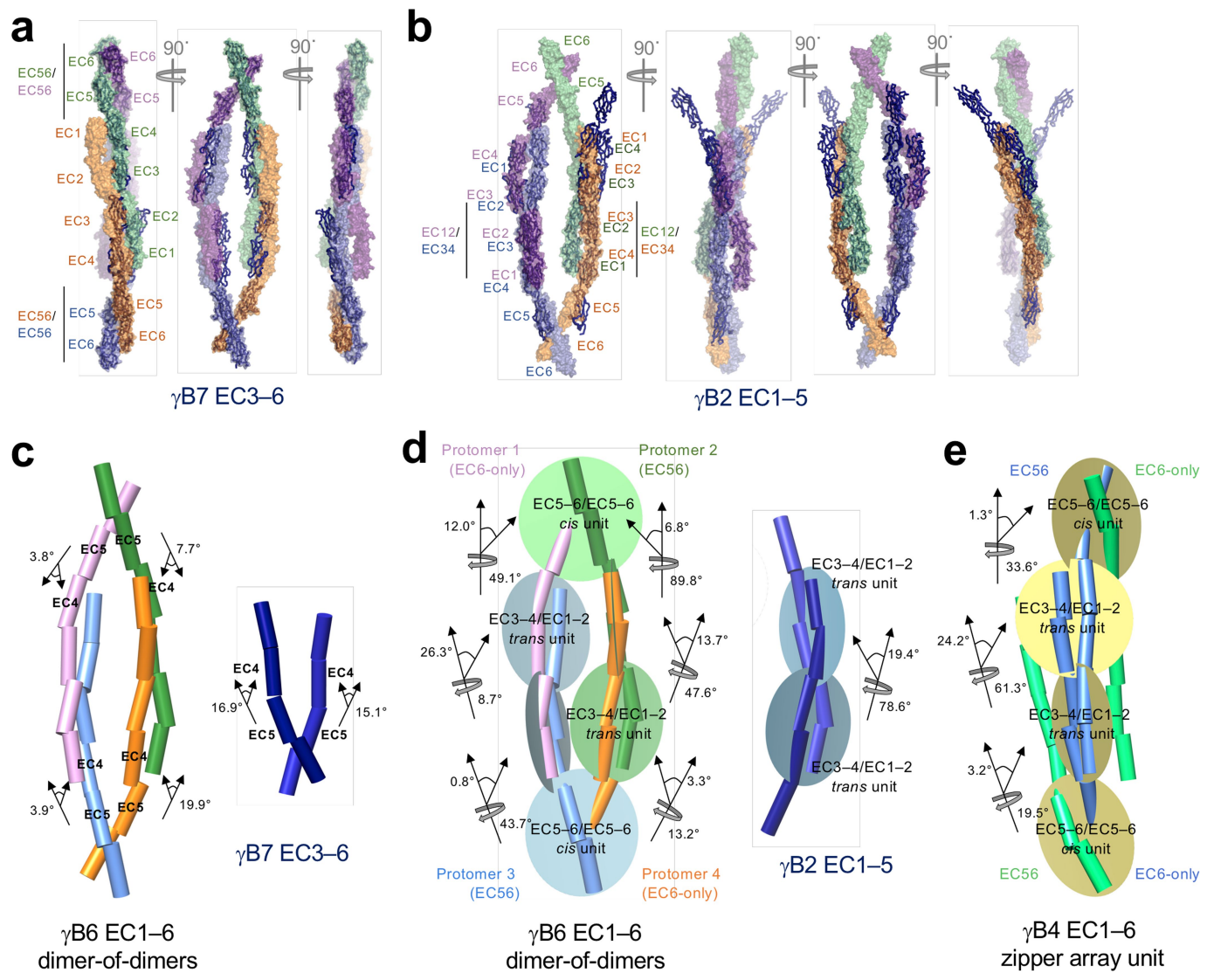
**Extended Data Fig. 3 | Particle selection and subtomogram averaging of cPCDH  $\gamma$ B6 complexes in solution.** **a**, Representative tomographic slice that shows the orientation of  $\gamma$ B6<sub>EC1-6</sub> complexes in vitreous ice. Note that front views are predominant, and represent a preferred orientation. Axis scale is in pixels. **b**, Complexes in the ice are selected as dipole

sets (blue sticks). For each particle ‘north’, ‘centre’ and ‘south’ points are marked as blue, cyan and red spheres, respectively. Axis scale is in pixels. **c**, Sub-volumes of pre-oriented particles were extracted from tomograms, and sub-tomogram averaged; projections of the final iteration after convergence are shown on the right.



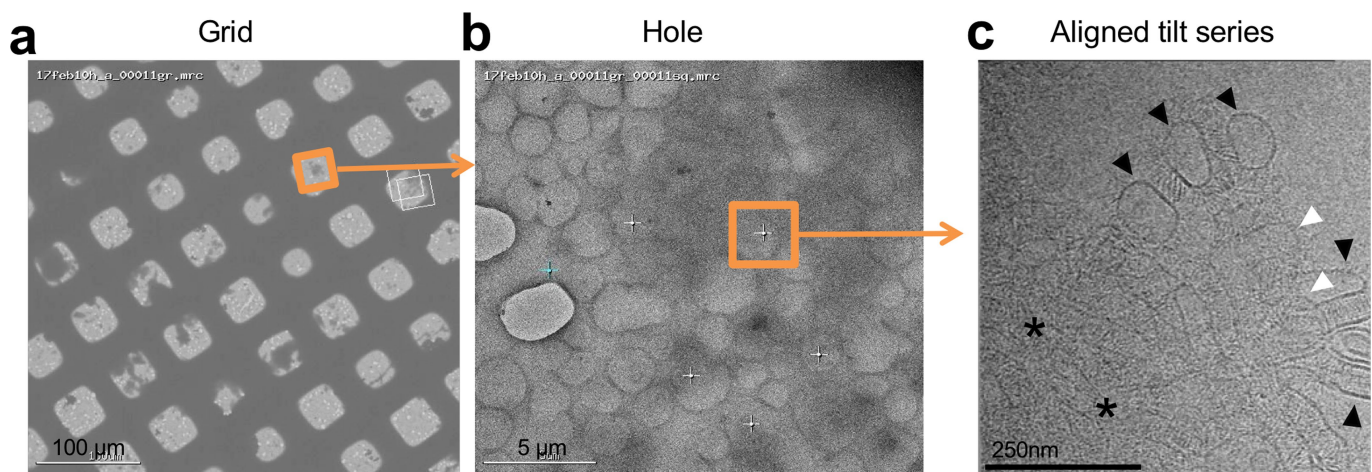
**Extended Data Fig. 4 | Two-dimensional cryo-electron microscopy of  $\gamma$ B6EC1-6 in solution.** **a**, Representative grid atlas of a grid prepared using Spotiton. Orange box highlights the path of sample deposition. **b**, Representative micrograph of  $\gamma$ B6EC1-6 in vitreous ice. Individual

extracellular cadherin domains are distinguishable within the ellipsoid particles. Orange boxes indicate representative particles. **c**, Two-dimensional class averages, calculated using Relion, show highly preferred orientation of  $\gamma$ B6EC1-6 in the ice. Five separate class averages are shown.



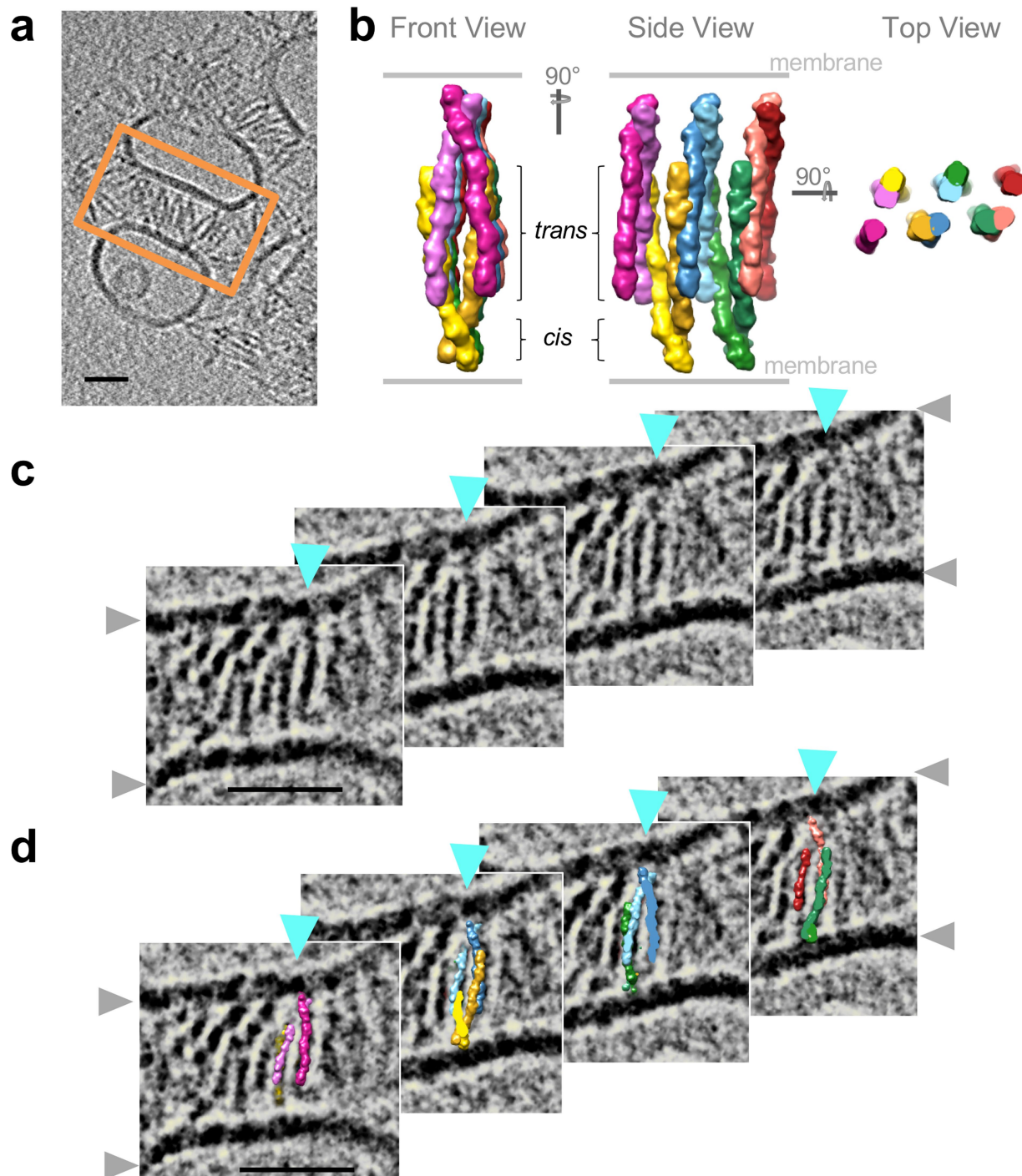
**Extended Data Fig. 5 | Structural comparisons of the dimer-of-dimers model from single-particle cryo-EM with crystallographic *cis* and *trans* dimers.** **a**, Crystallographic *cis* dimers of  $\gamma\text{B7}_{\text{EC3-6}}$  (blue ribbon) were aligned with the dimer-of-dimers model (space fill, colours as shown in Fig. 1) over the EC5–EC6 *cis*-dimer regions derived from  $\gamma\text{B7}_{\text{EC3-6}}$  (black bars). The EC4–EC5 linker region appears to accommodate a high degree of structural variation. **b**, Crystallographic  $\gamma\text{B2}_{\text{EC1-5}}$  *trans* dimers (blue ribbon) were aligned with the manually positioned EC1–EC2 and EC3–EC4 dimer fragments (black bars) in the dimer-of-dimers density. Deviations derive from differences in rotation and bend at the EC2–EC3 and EC3–EC4 linker regions within the antiparallel EC1–EC4 *trans* dimers. **c**, Comparison of the EC4–EC5 interdomain deflection angles between the dimer-of-dimers model (left) and the crystallographic  $\gamma\text{B7}_{\text{EC3-6}}$  *cis* dimer (right), highlighting the variations between them.

Individual extracellular cadherin domains were defined as axes in UCSF Chimera and are shown as cylinders. All interdomain deflection angles are listed in Extended Data Table 2. **d**, The dimer-of-dimers model was assembled by rigid-body-fitting into the cryo-ET density of four-domain *trans* (EC1–EC2 and EC3–EC4) and *cis* (EC5–EC6 and EC5–EC6) units from the  $\gamma\text{B2}_{\text{EC1-5}}$  and  $\gamma\text{B7}_{\text{EC3-6}}$  crystal structures, respectively. Deflection and rotational angles between these docked units in the final dimer-of-dimers model (left) compared with those in the  $\gamma\text{B2}_{\text{EC1-5}}$  *trans* dimer (right), highlighting the conformational change required within the EC1–EC4 *trans* interaction to facilitate formation of the dimer-of-dimers. **e**, Deflection and rotational angles between EC5–EC6 and EC5–EC6 *cis*-interaction and the EC3–EC4 and EC1–EC2 *trans*-interaction units in the repeating unit of the crystallographic  $\gamma\text{B4}_{\text{EC1-6}}$  zipper array, for comparison to the dimer-of-dimers model.



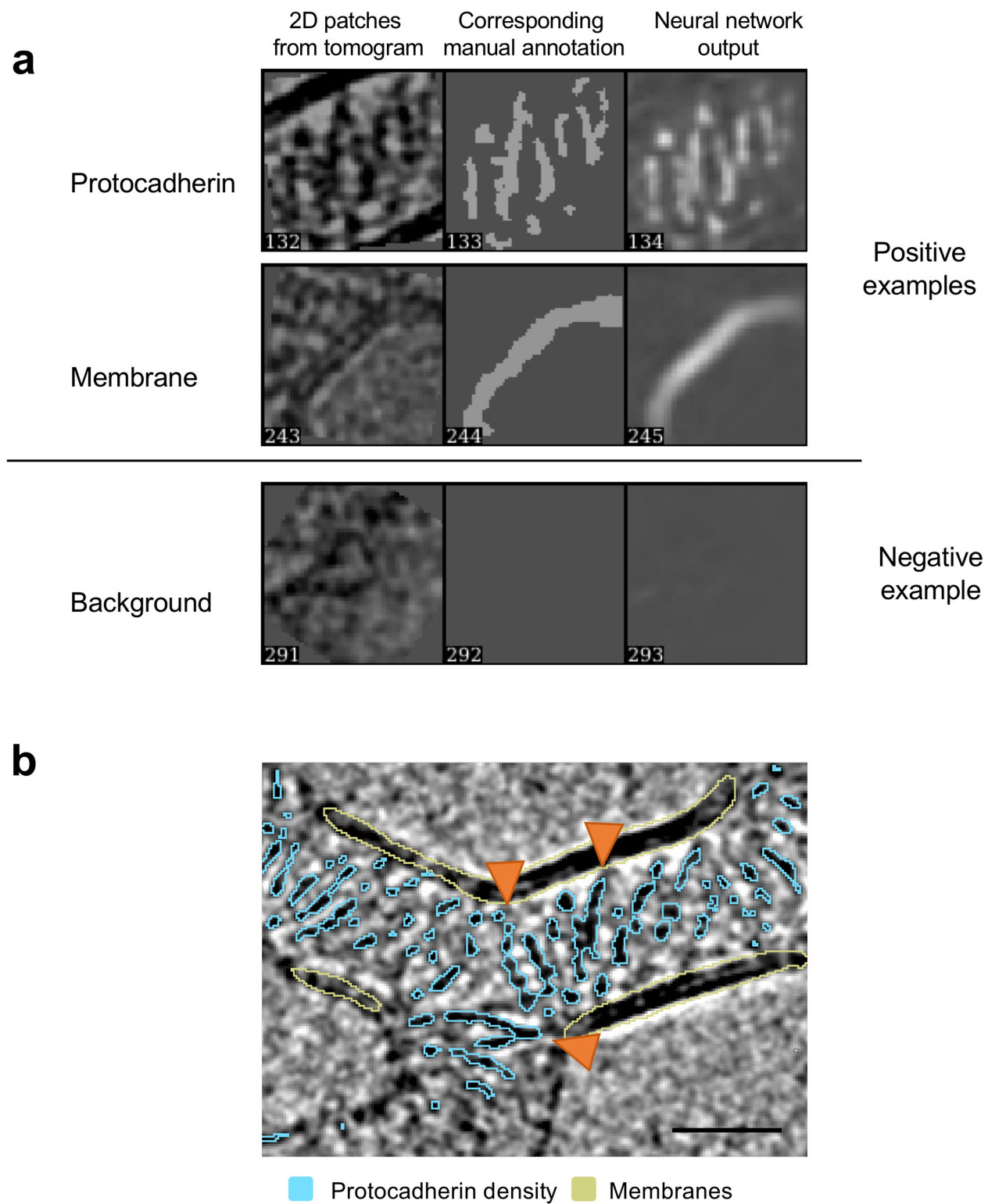
**Extended Data Fig. 6 | Data collection strategy for assessing protein assemblies formed by cPCDHs between liposomes.** **a**, Grid view of protein–liposome aggregates (dark shadows) deposited on lacey carbon grids, 300 copper mesh. **b**, Hole view of the boxed area shown in **a**. Protein–liposome aggregates can be seen as dark shadows. Tilt-series collection of liposome aggregates over lacey carbon holes in thin ice (orange square). White crosses represent additional data collection sites;

the cyan cross represents the focus target. **c**, Tilt image collected at the region highlighted in **b**. A single layer of liposomes coated in cPCDH density (black arrowhead), liposomes stacked on top of each other (white arrowhead) and—in addition—thick layers of stacked liposomes (asterisks) are visible in the image. Note that membranes at liposome contact sites appear to be parallel, and cPCDH density appears to be ordered. See Supplementary Video 2 for the reconstructed tomogram.



**Extended Data Fig. 7 | cPCDH zippers from the  $\gamma$ B4<sub>EC1-6</sub> crystal structure match the ordered linear arrays observed for  $\gamma$ B6<sub>EC1-6</sub> on membranes.** **a**, Tomographic slice through a reconstructed tomogram of adherent  $\gamma$ B6<sub>EC1-6</sub>-coated liposomes. The region of tomographic slices that is shown in close-up views in **c** and **d** is highlighted by an orange box. **b**, Molecular surface views of the  $\gamma$ B4<sub>EC1-6</sub> crystal lattice arrangement in three orientations. Each protomer is coloured in a different colour. **c**, Tomographic slices spanning 143 Å into the depth of the tomogram,

one linear array that progresses into the plane of the tomogram is indicated by cyan arrowheads. Grey arrowheads indicate lipid bilayers. **d**, Crystallographic  $\gamma$ B4<sub>EC1-6</sub> zipper consisting of five consecutive *cis* dimers placed into the cryo-ET density of the marked  $\gamma$ B6<sub>EC1-6</sub> array (cyan arrowheads) observed between membranes. Compare the density and structure fit between **c** and **d**. Protomers coloured as in **b**. Scale bars, 350 Å.



**Extended Data Fig. 8 | Automated tomogram annotation of cPCDH density and membranes.** **a**, Training and annotation of protein density and lipid bilayers. Examples of representative 2D-positive (top two panels) and -negative (bottom) annotations are shown. Left and middle, regions of interest on a tomographic slice (left) and manual annotation (middle) identify positive (white particles on black background) features.

Right, output after the training. A representative negative example is shown (bottom), in which no features are annotated by the trained neural network. **b**, Annotated tomographic slice. cPCDH density is shown in cyan, membranes in yellow. Orange arrowheads indicate single protomers to highlight examples of domain-level resolution of annotation. Scale bars, 350 Å.

Extended Data Table 1 | X-ray crystallography data collection and refinement statistics

Pcdh γB4 <sub>EC1–6</sub>		
<b>Data collection</b>		
Date	12/01/2016	
Beamline	APS 24ID-C	
Wavelength (Å)	0.97919	
Space group	<i>P</i> 2 <sub>1</sub>	
<i>Cell dimensions</i>		
a, b, c (Å)	127.73, 87.58, 149.33	
α, β, γ (°)	90, 109.94, 90	
<i>Spherical resolution limits</i>		<i>Ellipsoidal resolution limits</i>
Resolution (Å)	40.00–4.50 (5.03–4.50)	40–6.0/6.8/4.5 (5.05–4.52)
No. of reflections	49398 (13826)	24717 (966)
Unique reflections	17427 (4999)	8694 (317)
R <sub>merge</sub>	0.207 (1.921)	0.112 (0.173)
R <sub>meas</sub>	0.254 (2.366)	0.138 (0.211)
R <sub>pim</sub>	0.145 (1.359)	0.078 (0.119)
CC(1/2)	0.993 (0.741)	0.995 (0.973)
I/σI	2.7 (0.6)	5.2 (5.7)
Spherical completeness (%)	93.8 (94.9)	46.7 (5.6)
Ellipsoidal completeness (%)		93.6 (97.2)
Redundancy	2.8 (2.8)	2.8 (3.0)
<b>Refinement</b>		
Resolution (Å)	40–6.0/6.8/4.5	
Unique reflections	8683	
Completeness in diffracting ellipsoid (%)	93.4	
R <sub>work</sub> / R <sub>free</sub> (%)	23.1 / 27.7	
Molecules in A.S.U.	2	
<i>Number of atoms</i>		
Protein	9489	
Ligand/Ion	253	
Water	0	
<i>B-factors</i>		
Protein	138.19	
Ligand/Ion	157.81	
Water	0	
<i>R.m.s. deviations</i>		
Bond lengths (Å)	0.002	
Bond angles (°)	0.565	
<i>Ramachandran</i>		
Favored (%)	96.96	
Allowed (%)	3.04	
Outliers (%)	0.00	
Rotamer outliers (%)	0.67	
Wilson B	66.09	
PDB ID	6E6B	

Values in parentheses are for the outer shell. APS, Advanced Photon Source, Argonne National Laboratory; A.S.U., asymmetric unit; R.m.s., Root mean square. See Extended Data Fig. 1 and Methods for further details on the ellipsoidal resolution limits.

## Extended Data Table 2 | Interdomain angles

Interdomain angles	EC1:EC2 (°)	EC2:EC3 (°)	EC3:EC4 (°)	EC4:EC5 (°)	EC5:EC6 (°)
<b><u><math>\gamma</math>B-Pcdh trans-dimer structures</u></b>					
$\gamma$ B2 <sub>EC1-5</sub> chain A	19.9	9.5	15.7	13.9	
$\gamma$ B2 <sub>EC1-5</sub> chain B	21.5	9	15.4	16.3	
$\gamma$ B3 <sub>EC1-4</sub>	8.6	11.3	17.2		
$\gamma$ B7 <sub>EC1-4</sub> crystal form 1 chain A	11.2	5	13.2		
$\gamma$ B7 <sub>EC1-4</sub> crystal form 1 chain B	11.2	8.2	13.4		
$\gamma$ B7 <sub>EC1-4</sub> crystal form 2 chain A	5.2	3.7	8.5		
$\gamma$ B7 <sub>EC1-4</sub> crystal form 2 chain B	13.6	6.9	14.6		
Average $\gamma$ B trans dimer	13.0 ± 5.9	7.7 ± 2.6	14.0 ± 2.8	15.1 ± 1.7	
<b><u><math>\gamma</math>B7 cis-dimer structure</u></b>					
$\gamma$ B7 <sub>EC3-6</sub> chain A (EC6-only)			8.1	15.1	12.5
$\gamma$ B7 <sub>EC3-6</sub> chain D (EC5-6)			8.5	16.9	14.6
$\gamma$ B7 <sub>EC3-6</sub> chain B (EC5-6)			14.8	15.3	19.1
$\gamma$ B7 <sub>EC3-6</sub> chain C (EC6-only)			11.3	14.3	11
Average $\gamma$ B7 cis dimer			10.7 ± 3.1	15.4 ± 1.1	14.3 ± 3.5
<b><u><math>\gamma</math>B4 zipper crystal structure</u></b>					
$\gamma$ B4 <sub>EC1-6</sub> chain A (EC6-only)	6.7	6.7	11	19.8	16.7
$\gamma$ B4 <sub>EC1-6</sub> chain B (EC5-6)	6.6	4.4	9.7	14.3	18.8
Average $\gamma$ B4 zipper	6.7 ± 0.1	5.6 ± 1.6	10.4 ± 0.9	17.1 ± 3.9	17.8 ± 1.5
<b><u>Single particle cryo-ET <math>\gamma</math>B6 dimer-of-dimers model</u></b>					
$\gamma$ B6 <sub>EC1-6</sub> protomer 1 (EC6-only)	21.5	15.5	15.7	3.8	12.5
$\gamma$ B6 <sub>EC1-6</sub> protomer 2 (EC5-6)	21.5	5.1	15.7	7.7	14.6
$\gamma$ B6 <sub>EC1-6</sub> protomer 3 (EC5-6)	21.5	30.5	15.7	3.9	19.1
$\gamma$ B6 <sub>EC1-6</sub> protomer 4 (EC6-only)	21.5	23.3	15.7	19.9	11.0
Average dimer-of-dimers	21.5 ± 0.0*	18.6 ± 10.9	15.7 ± 0.0*	8.8 ± 7.6	14.3 ± 3.5*

Interdomain deflection angles between consecutive extracellular cadherin domains are given as the deviation from 180°. Angles were calculated using UCSF Chimera. The  $\gamma$ B2<sub>EC1-5</sub>,  $\gamma$ B3<sub>EC1-4</sub>,  $\gamma$ B7<sub>EC1-4</sub> crystal form 1,  $\gamma$ B7<sub>EC1-4</sub> crystal form 2 and  $\gamma$ B7<sub>EC3-6</sub> structures correspond to PDB 5T9T, 5K8R, 5SZO, 5SZP and 5V5X, respectively.

\*The dimer-of-dimers model was generated using four-domain rigid interaction units; four copies of EC1-EC2 and EC3-EC4 from  $\gamma$ B2<sub>EC1-5</sub> and the two EC5-EC6/EC5-EC6 units from the  $\gamma$ B7<sub>EC3-6</sub> crystal structure. The EC1-EC2, EC3-EC4 and EC5-EC6 angles are, therefore, unchanged.

## Reporting Summary

Nature Research wishes to improve the reproducibility of the work that we publish. This form provides structure for consistency and transparency in reporting. For further information on Nature Research policies, see [Authors & Referees](#) and the [Editorial Policy Checklist](#).

### Statistical parameters

When statistical analyses are reported, confirm that the following items are present in the relevant location (e.g. figure legend, table legend, main text, or Methods section).

n/a Confirmed

- The exact sample size (n) for each experimental group/condition, given as a discrete number and unit of measurement
- An indication of whether measurements were taken from distinct samples or whether the same sample was measured repeatedly
- The statistical test(s) used AND whether they are one- or two-sided  
*Only common tests should be described solely by name; describe more complex techniques in the Methods section.*
- A description of all covariates tested
- A description of any assumptions or corrections, such as tests of normality and adjustment for multiple comparisons
- A full description of the statistics including central tendency (e.g. means) or other basic estimates (e.g. regression coefficient) AND variation (e.g. standard deviation) or associated estimates of uncertainty (e.g. confidence intervals)
- For null hypothesis testing, the test statistic (e.g.  $F$ ,  $t$ ,  $r$ ) with confidence intervals, effect sizes, degrees of freedom and  $P$  value noted  
*Give P values as exact values whenever suitable.*
- For Bayesian analysis, information on the choice of priors and Markov chain Monte Carlo settings
- For hierarchical and complex designs, identification of the appropriate level for tests and full reporting of outcomes
- Estimates of effect sizes (e.g. Cohen's  $d$ , Pearson's  $r$ ), indicating how they were calculated
- Clearly defined error bars  
*State explicitly what error bars represent (e.g. SD, SE, CI)*

*Our web collection on [statistics for biologists](#) may be useful.*

### Software and code

Policy information about [availability of computer code](#)

Data collection

Crystallographic data collection: RAPD from NECAT  
Electron microscopy data collection: Leginon

Data analysis

Signal Peptide prediction: SignalP 4.0 Server  
Crystallographic data processing: XDS, XSCALE, CCP4, Aimless, UCLA Diffraction Anisotropy Server, Phaser, Coot, Phenix  
Electron microscopy/tomography data processing: Leginon, MotionCor2, RELION2, Cryosparc, Appion-Protomo including the Tomo 3D SIRT software, Dynamo, Topaz  
Docking of structures into cryo-electron tomography maps: Chimera  
Tomogram annotation: TomoSeg in EMAN2.2  
Figures were prepared using: Chimera, PyMol, Amira

For manuscripts utilizing custom algorithms or software that are central to the research but not yet described in published literature, software must be made available to editors/reviewers upon request. We strongly encourage code deposition in a community repository (e.g. GitHub). See the Nature Research [guidelines for submitting code & software](#) for further information.

## Data

Policy information about [availability of data](#)

All manuscripts must include a [data availability statement](#). This statement should provide the following information, where applicable:

- Accession codes, unique identifiers, or web links for publicly available datasets
- A list of figures that have associated raw data
- A description of any restrictions on data availability

Crystallographic atomic coordinates and structure factors have been deposited in the protein data bank with accession code PDB: 6E6B.

Electron microscopy data has been deposited to the relevant databases:

Binned by four or two tomograms of the single-particle and Pcdh-liposome datasets were deposited in the Electron Microscopy Data bank (EMDB) with accession codes: EMD-9197, EMD-9198, EMD-9199 and EMD-9200.

Single particle data, unaligned tilt-series images, Appion-Protomo tilt-series alignment runs, and aligned tilt-series stacks were deposited to the Electron Microscopy Pilot Image Archive (EMPIAR) with accession codes: EMPIAR-10234, EMPIAR-10235, EMPIAR-10236, EMPIAR-10237, and EMPIAR-10238.

All of these data will be made available to reviewers upon request.

## Field-specific reporting

Please select the best fit for your research. If you are not sure, read the appropriate sections before making your selection.

Life sciences       Behavioural & social sciences       Ecological, evolutionary & environmental sciences

For a reference copy of the document with all sections, see [nature.com/authors/policies/ReportingSummary-flat.pdf](http://nature.com/authors/policies/ReportingSummary-flat.pdf)

## Life sciences study design

All studies must disclose on these points even when the disclosure is negative.

Sample size	Crystallographic data was obtained from a single crystal. 14,569 particles were used for 2D classification for single-particle electron microscopy. 506 particles were picked from seven different tomograms to produce the sub-tomogram averaged map. Sample sizes were determined based on prior literature and best practices in the field; no statistical methods were used to predetermine sample size.
Data exclusions	No data were excluded.
Replication	Liposome aggregation assays were replicated in three independent experiments and gave highly consistent results. The appearance of all electron microscopy protein and protein/liposome samples were highly reproducible. Reconstructed tomograms of wild-type and mutant proteins coated onto liposomes, are from at least $n > 3$ independent experiments. Ordered assemblies were consistently observed in all wild-type Pcdh experiments, while the ordered assemblies were consistently absent in all cis-mutant Pcdh tiltseries.
Randomization	Randomization is not relevant to a structural study.
Blinding	Blinding is not relevant to a structural study.

## Reporting for specific materials, systems and methods

### Materials & experimental systems

n/a	Involved in the study
<input type="checkbox"/>	<input checked="" type="checkbox"/> Unique biological materials
<input checked="" type="checkbox"/>	<input type="checkbox"/> Antibodies
<input type="checkbox"/>	<input checked="" type="checkbox"/> Eukaryotic cell lines
<input checked="" type="checkbox"/>	<input type="checkbox"/> Palaeontology
<input checked="" type="checkbox"/>	<input type="checkbox"/> Animals and other organisms
<input checked="" type="checkbox"/>	<input type="checkbox"/> Human research participants

### Methods

n/a	Involved in the study
<input checked="" type="checkbox"/>	<input type="checkbox"/> ChIP-seq
<input checked="" type="checkbox"/>	<input type="checkbox"/> Flow cytometry
<input checked="" type="checkbox"/>	<input type="checkbox"/> MRI-based neuroimaging

## Unique biological materials

Policy information about [availability of materials](#)

Obtaining unique materials      Plasmid expression constructs used for protein production available upon request.

## Eukaryotic cell lines

Policy information about [cell lines](#)

Cell line source(s) HEK-293F (FreeStyle) cells used for protein production were obtained from Thermo Fisher.

Authentication Cell line has been authenticated by the vendor.

Mycoplasma contamination Cells were not tested for mycoplasma contamination

Commonly misidentified lines  
(See [ICLAC](#) register) Cells are not listed in the database.